

# AMO-HEAD: Adaptive MARG-Only Heading Estimation for UAVs under Magnetic Disturbances

Qizhi Guo, Siyuan Yang, Junning Lyu, Jianjun Sun, Defu Lin, Shaoming He\*

**Abstract**—Accurate and robust heading estimation is crucial for unmanned aerial vehicles (UAVs) when conducting indoor inspection tasks. However, the cluttered nature of indoor environments often introduces severe magnetic disturbances, which can significantly degrade heading accuracy. To address this challenge, this paper presents an Adaptive MARG-Only Heading (AMO-HEAD) estimation approach for UAVs operating in magnetically disturbed environments. AMO-HEAD is a lightweight and computationally efficient Extended Kalman Filter (EKF) framework that leverages inertial and magnetic sensors to achieve reliable heading estimation. In the proposed approach, gyroscope angular rate measurements are integrated to propagate the quaternion state, which is subsequently corrected using accelerometer and magnetometer data. The corrected quaternion is then used to compute the UAV’s heading. An adaptive process noise covariance method is introduced to model and compensate for gyroscope measurement noise, bias drift, and discretization errors arising from the Euler method integration. To mitigate the effects of external magnetic disturbances, a scaling factor is applied based on real-time magnetic deviation detection. A theoretical observability analysis of the proposed AMO-HEAD is performed using the Lie derivative. Extensive experiments were conducted in real world indoor environments with customized UAV platforms. The results demonstrate the effectiveness of the proposed algorithm in providing precise heading estimation under magnetically disturbed conditions.

**Index Terms**—Heading estimation, magnetic disturbance, adaptive extended Kalman filter, observability analysis

## I. INTRODUCTION

The deployment of autonomous UAVs for inspection tasks within industrial facilities is becoming increasingly prevalent [1]. A critical requirement for these applications is precise heading [2], which is essential for maintaining a stable sensor field-of-view on inspection targets. Unlike roll and pitch, which can be accurately determined using, UAVs heading typically relies on magnetometer readings of the Earth’s magnetic field. However, confined indoor environments are often characterized by significant magnetic disturbances originating from industrial equipment. These disturbances corrupt magnetometer measurements and degrade heading accuracy [3]. Consequently, achieving robust heading estimation under these conditions is paramount for reliable autonomous inspection.

The absence of reliable satellite navigation signals indoors [4] precludes the use of satellite-based heading determination.

This work was supported by the National Natural Science Foundation of China under Grant No. 52302449.

Qizhi Guo, Siyuan Yang, Junning Lyu, Defu Lin, Shaoming He are with the School of Aerospace Engineering, Beijing Institute of Technology, Beijing, 100081, China.

Jianjun Sun is with the Beijing Aerospace Automatic Control Institute, Beijing, 100854, China.

\*Corresponding author. Email: shaoming.he@bit.edu.cn

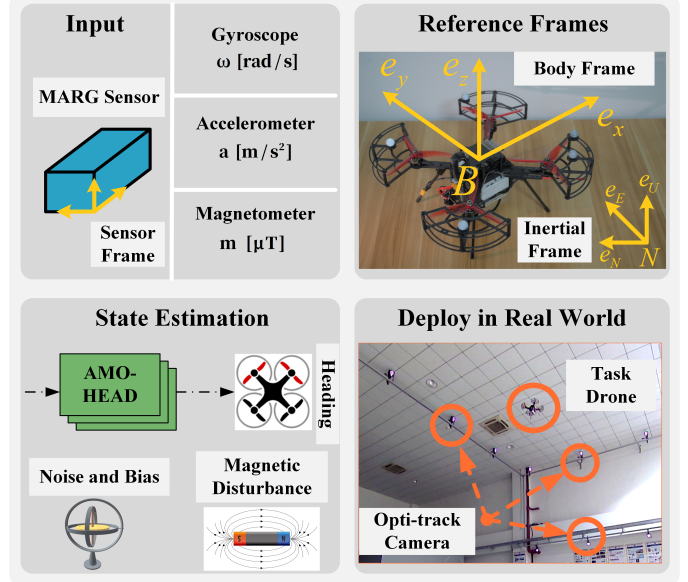


Fig. 1: The illustration of the AMO-HEAD heading estimation framework. Raw gyroscope, accelerometer and magnetometer measurements from a MARG sensor are fused in real time while actively suppressing magnetic disturbances. The resulting robust heading estimates enable reliable UAV inspection under magnetic field distortions.

Alternative modalities, such as LiDAR and vision, also present challenges in industrial settings due to insufficient strong and stable features. LiDAR-based methods [5, 6] can fail in feature-sparse environments, a problem exacerbated by the limited field of view of some sensors. Similarly, visual-inertial odometry (VIO) systems [7–9] demand robust visual features and significant computational resources, limiting their feasibility on small, resource-constrained UAVs. Given these limitations, the fusion of data from MARG sensors, i.e., Magnetic, Angular Rate, and Gravity sensors, offers a compelling alternative for UAV heading estimation [10–12]. MARG sensors provide lightweight and self-contained heading estimation independent of environmental features. However, estimators relying solely on an Inertial Measurement Unit (IMU) accumulate unbounded heading errors over time due to uncompensated gyroscope bias drift [13]. While filter-based fusion of IMU and magnetometer data can mitigate long-term drift, conventional methods often depend on fixed noise-covariance parameters [14], rendering them unable to adapt to dynamic magnetic disturbances. Therefore, the accurate modeling and compensation of these dynamic errors are critical

for enhancing sensor fusion reliability.

This paper presents AMO-HEAD, as shown in Fig. 1, a quaternion-based adaptive Extended Kalman Filter (AEKF) framework designed for robust UAV heading estimation under magnetically disturbed indoor environments. The proposed method achieves real-time performance on embedded processors by focusing on magnetic disturbance suppression without reliance on external references. The key contributions of this work are threefold:

- The development of a lightweight, computationally efficient AEKF that fuses MARG sensor data to achieve accurate heading estimation.
- The formulation of an adaptive process noise covariance model to account for gyroscope measurement noise, bias drift, and discretization errors, coupled with a scaling factor that dynamically adjusts the measurement noise covariance in response to detected magnetic disturbances.
- An extensive experimental validation on customized UAV platforms with synchronized ground truth, demonstrating the robustness of AMO-HEAD in cluttered and magnetically disturbed indoor environments.

The rest of this paper is organized as follows. Section II reviews related research. Section III presents the theoretical background. Section IV details the proposed algorithm and its key components. Section V provides the system observability analysis. Section VI reports on real world experiments and benchmark comparisons, followed by conclusions in Section VII.

## II. RELATED WORKS

Approaches to MARG sensor heading estimation fall into two categories, filter-based and learning-based methods. Filter-based methods comprise complementary filter (CF) and Kalman filter (KF) variants built on explicit kinematic models, whereas learning-based methods infer heading directly from data. We review representative CF/KF approaches and then briefly outline recent learning-based studies, positioning our adaptive EKF within this landscape.

### A. Complementary Filter-Based Heading Estimation

CF-based method is one of the most prevalent approaches to achieve heading estimation in robotics applications. These optimization-based methods [15–17] iteratively minimize an error function to refine the orientation estimate and leverage gradient descent to fine-tune parameters through iterative process. For instance, the authors in [18] introduced an efficient orientation filter using a gradient descent algorithm (GDA) to find an optimal quaternion from accelerometer and magnetometer data, which then corrects the gyroscope-propagated orientation. While effective, the iterative optimization and manually tuned gain parameters can impose a significant computational burden. Later in [19], the authors enhanced the algorithm in [18] for controlling a robotic manipulator by decoupling magnetic field variance from roll and pitch estimation. However, this implementation relied on substantial computational resources with a large onboard computer. In the underwater domain, a similar CF-based strategy requires

a costly Fiber Optic Gyroscope (FOG) to maintain heading accuracy under magnetic disturbances [20]. The work [21] presented an orientation estimation framework for UAVs using an adaptive CF implemented directly on the  $SO(3)$  manifold. The suggested adaptive mechanism adjusts MARG sensor contributions in response to external magnetic disturbances and data inconsistencies. Nevertheless, A key limitation of such  $SO(3)$ -based CFs is their reliance on heuristically tuned parameters and their lack of an explicit model for sensor noise statistics.

### B. Kalman Filter-Based Heading Estimation

In contrast, KF-based methods are probabilistic state estimators that recursively update the orientation based on a system model and incoming measurements [22]. Since the computation complexity of the CF grows rapidly with the number of system dimensions and sensor data, KF and its nonlinear variants are often preferred for their rigorous handling of system dynamics and noise statistics [23]. The authors in [24] applied an Unscented Kalman Filter (UKF) for attitude and bias estimation on a fixed-wing UAV using Euler angle parameterization. However, UKF-based algorithms are still computationally intensive. An EKF-based attitude estimation method for quadrotors with a switching strategy that selects among multiple filter modes to adapt to different flight dynamics is proposed in [25], achieving both high accuracy and computational efficiency for onboard implementation. A critical limitation of conventional KF-based approaches is their reliance on a priori, static noise covariance matrices [26]. To address this, some have explored detect-and-reject mechanisms, as demonstrated on ground robots for mitigating magnetic disturbances [27]. This approach is ultimately limited by its reliance on rigid, empirically-tuned thresholds that fail to generalize to new environments.

In parallel with the filter-based pipelines, recent data-driven methods learn heading from MARG sensor signals. MARG-supervised models report low heading errors under harsh conditions when training and deployment domains are matched [28–30]. IMU denoising networks reduce gyro drift and yield accurate heading estimates [31, 32]. Besides, heading can be inferred within data-driven odometry, which learn motion dynamics directly from inertial streams [33–35]. While accurate in domain, these approaches typically require substantial labeled data and can suffer generalization issues across robot platforms, sampling rates, and especially indoor magnetic environments. In contrast to data-driven methods, this paper proposes AMO-HEAD. It is a training-free and physics-guided framework that explicitly fuses MARG sensor measurements. Rather than using static covariances in conventional EKFs, AMO-HEAD enhances robustness by adaptively tuning the gyroscope process noise online. Furthermore, it scales the magnetometer measurement covariance based on residuals to suppress transient outliers without hard rejection. This lightweight and adaptive design requires no training, enabling robust, real-time heading estimation on resource-constrained UAVs.

### III. PRELIMINARIES AND BACKGROUNDS

Since direct measurement of the heading angle using magnetic sensors is highly susceptible to environmental interference, especially in indoor spaces filled with electronic equipment. An alternative and robust approach is to estimate the full 3-D orientation and then extract the heading component. This section first introduces the quaternion kinematics and the MARG sensor models. Finally, the problem to be solved of this paper will be presented.

#### A. Quaternion Kinematics Model

This work utilizes an inertial frame  $\{n\}$  and a body frame  $\{b\}$  to describe the UAV's motion, as shown in Fig. 1. The orientation of the body frame relative to the inertial frame is represented by quaternions. Detailed descriptions of the coordinate systems are provided in Appendix A. The true orientation of the UAV in the inertial frame is represented by the MARG sensor frame relative to the inertial frame, which is specified by the unit quaternion

$$\mathbf{q} = [q_w \ q_x \ q_y \ q_z]^T \quad (1)$$

where  $q_w$  is the scalar part and  $q_x, q_y, q_z$  are the vector parts of the quaternion. Unlike Euler angles, quaternions are chosen for the attitude representation since they provide a singularity-free representation of 3-D rotations and hence avoid the ambiguity (such as gimbal lock). The continuous-time kinematics of the quaternion can be expressed by [36]

$$\dot{\mathbf{q}} = \frac{1}{2} \mathbf{q} \otimes \boldsymbol{\omega} = \frac{1}{2} \boldsymbol{\Omega}(\boldsymbol{\omega}) \mathbf{q} \quad (2)$$

where  $\otimes$  denotes the quaternion multiplication;  $\boldsymbol{\omega} = [\omega_x, \omega_y, \omega_z]^T \in \mathbb{R}^3$  stands for the angular rate; and  $\boldsymbol{\Omega}(\boldsymbol{\omega})$  is a skew-symmetric matrix constructed from the angular velocity, used to express the quaternion differential equation in a linear form. It is defined as

$$\boldsymbol{\Omega}(\boldsymbol{\omega}) = \begin{bmatrix} \mathbf{0} & -\boldsymbol{\omega}^T \\ \boldsymbol{\omega} & [\boldsymbol{\omega} \times] \end{bmatrix} \quad (3)$$

where  $[\boldsymbol{\omega} \times]$  denotes the cross-product matrix with

$$[\boldsymbol{\omega} \times] = \begin{bmatrix} 0 & \omega_z & -\omega_y \\ -\omega_z & 0 & \omega_x \\ \omega_y & -\omega_x & 0 \end{bmatrix} \quad (4)$$

The UAV's heading angle  $\psi$  is defined as the angle from the north direction to the UAV's forward direction, measured clockwise in the ENU frame. The relationship between the UAV's heading angle  $\psi$  and the quaternion is given by

$$\psi = \arctan \left[ \frac{2(q_w q_z + q_x q_y)}{1 - 2(q_y^2 + q_z^2)} \right] \quad (5)$$

#### B. MARG Sensor Model

The MARG sensor unit consists of a gyroscope, an accelerometer and a magnetometer. Let  $\boldsymbol{\omega}_g \in \mathbb{R}^3$ ,  $\mathbf{y}_a \in \mathbb{R}^3$ ,  $\mathbf{y}_m = [y_{mx} \ y_{my} \ y_{mz}] \in \mathbb{R}^3$  be the outputs of the aforementioned sensors, respectively. Gyroscopes are subject to inherent bias, which refers to a slowly varying offset present in the output even when there is no actual rotation.

Mathematically, the measured angular velocity can be modeled as

$$\boldsymbol{\omega}_g = \boldsymbol{\omega} + \mathbf{b}_g + \mathbf{v}_\omega \quad (6)$$

where  $\mathbf{b}_g$  represents the gyroscope bias, and  $\mathbf{v}_\omega$  is the zero-mean Gaussian measurement noise with covariance as  $\boldsymbol{\Sigma}_\omega$ . The gyroscope bias kinematics is modeled as a white noise driven random walk

$$\dot{\mathbf{b}}_g = \mathbf{v}_b \quad (7)$$

where  $\mathbf{v}_b$  represents zero-mean Gaussian white noise with covariance  $\boldsymbol{\Sigma}_b$ .

The accelerometer and magnetometer provide measurements that can be modeled as observations of the gravity and local magnetic field vectors, which can be transformed into the body frame by current rotation matrix using

$$\begin{aligned} \mathbf{y}_a &= \mathbf{h}_{acc}(\mathbf{q}) = \mathbf{C}(\mathbf{q}) \mathbf{g} + \mathbf{v}_a \\ \mathbf{y}_m &= \mathbf{h}_{mag}(\mathbf{q}) = \mathbf{C}(\mathbf{q}) \mathbf{m} + \mathbf{v}_m \end{aligned} \quad (8)$$

where the sensor noises  $\mathbf{v}_a \in \mathbb{R}^3$ , and  $\mathbf{v}_m \in \mathbb{R}^3$  are assumed to be uncorrelated Gaussian white noise with covariance matrices  $\mathbf{R}_a$  and  $\mathbf{R}_m$ , respectively. The Earth's gravity vector  $\mathbf{g}$  and magnetic field vector  $\mathbf{m}$  are determined by  $\mathbf{g} = [0 \ 0 \ g]^T$  and  $\mathbf{m} = [m_x^r \ m_y^r \ m_z^r]^T$ , with  $g$  being the gravitational acceleration and  $m^r$  being the local reference magnetic field magnitude. The rotation matrix  $\mathbf{C}(\mathbf{q})$  with its full expression is detailed in Appendix A. Based on sensor models introduced in Eq. (8), the accelerometer and magnetometer measurement model can be represented by a compact form as

$$\mathbf{z} = \mathbf{h}(\mathbf{q}) + \mathbf{v} = \begin{bmatrix} \mathbf{C}(\mathbf{q}) & \mathbf{0}_{3 \times 3} \\ \mathbf{0}_{3 \times 3} & \mathbf{C}(\mathbf{q}) \end{bmatrix} \begin{bmatrix} \mathbf{g} \\ \mathbf{m} \end{bmatrix} + \mathbf{v} \quad (9)$$

where  $\mathbf{z}$  is the measurement vector that stacks the accelerometer and magnetometer readings in the body frame as  $\mathbf{z} = [\mathbf{y}_a^T \ \mathbf{y}_m^T]^T$ , and  $\mathbf{v}$  is the measurement noise vector, defined as  $\mathbf{v} = [\mathbf{v}_a^T \ \mathbf{v}_m^T]^T$ . The measurement noise covariance matrix  $\mathbf{R}_t$  is given by

$$\mathbf{R}_t = \begin{bmatrix} \mathbf{R}_a & \mathbf{0}_{3 \times 3} \\ \mathbf{0}_{3 \times 3} & \mathbf{R}_m \end{bmatrix} \quad (10)$$

#### C. Problem Description

It follows from Eq. (5) that the problem of heading estimation can be reformulated as a quaternion-based orientation estimation problem. Hence, the main objective of this paper is to estimate  $\mathbf{q}$  using the MARG sensor measurements  $\boldsymbol{\omega}_g$ ,  $\mathbf{y}_a$ ,  $\mathbf{y}_m$ . Specifically, the quaternion propagation utilizes the angular rate measurement  $\boldsymbol{\omega}_g$  from the gyroscope, while the estimation update relies on the accelerometer and magnetometer measurements  $\mathbf{y}_a$ ,  $\mathbf{y}_m$ . Once we have  $\mathbf{q}$ , the heading can be readily extracted from Eq. (5). Since the gyroscope measurement  $\boldsymbol{\omega}_g$ , as defined in Eq. (6), is corrupted by the unknown bias  $\mathbf{b}_g$ , we augment the bias into the estimation state as  $\mathbf{x} = [\mathbf{q}^T \ \mathbf{b}_g^T]^T \in \mathbb{R}^7$ . Then, the nonlinear dynamics model can be readily formulated using Eqs. (2) and (7) as

$$\dot{\mathbf{x}} = \mathbf{f}(\mathbf{x}) = \begin{bmatrix} \frac{1}{2} \boldsymbol{\Omega}(\boldsymbol{\omega}) \mathbf{q} \\ \mathbf{0} \end{bmatrix} \quad (11)$$

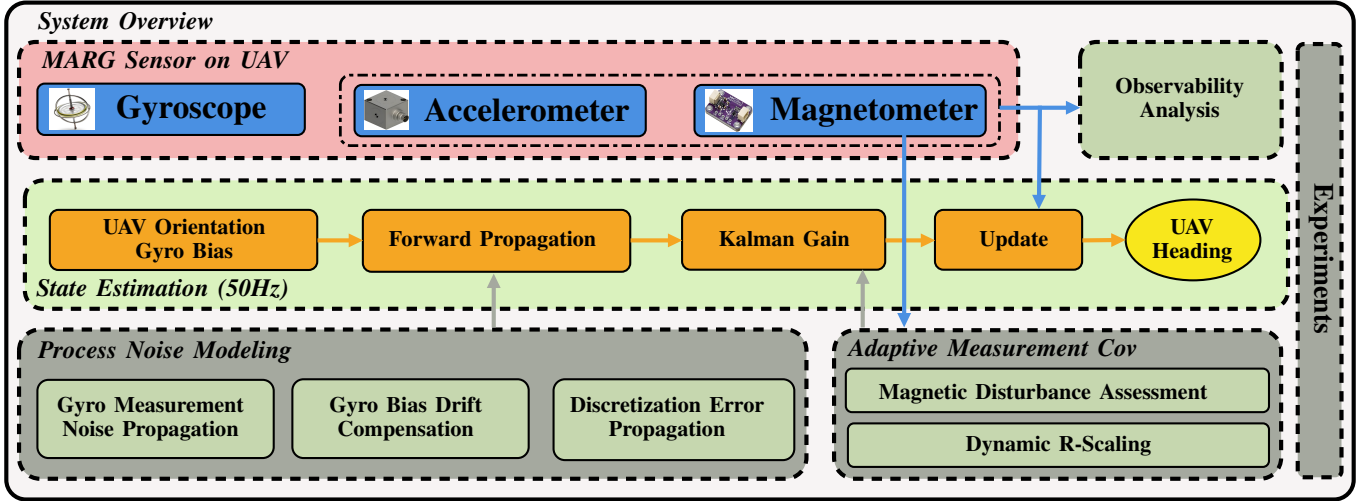


Fig. 2: System overview of the proposed heading estimation framework.

**Problem 1.** Given the nonlinear dynamics (11) and noise-corrupted nonlinear measurement (9), design a proper EKF to estimate  $\mathbf{x}$ .

Although the unknown bias can be estimated partially rejected in the quaternion propagation by using the augmented dynamics model, the gyroscope measurement noise  $\mathbf{v}_\omega$  still introduces additional uncertainties in the quaternion propagation. Furthermore, magnetometer measurements in indoor environments suffer from time varying magnetic disturbances. Therefore, how to characterize sensor-related process noise and adaptively compensate for real-time magnetic disturbances is key to solve Problem 1.

#### IV. AMO-HEAD: ADAPTIVE STATE ESTIMATION

In this section, we present the detailed design and implementation of the proposed AMO-HEAD for UAV heading estimation. The overview of our system is shown in Fig. 2. First, the quaternion-based filter design and state space formulation are introduced. Subsequently, an adaptive strategy for characterizing process noise covariance is described to handle gyroscope noise, bias drift, and discretization errors. Finally, we develop an adaptive measurement noise covariance mechanism to compensate for varying magnetic disturbances in real time.

##### A. Filter Design

The magnetometer readings are fused with the accelerometer and gyroscope readings to estimate the UAV's heading by the proposed AEKF-based estimator. The AEKF operates through the standard prediction-update cycle.

1) *Quaternion Propagation:* To compute the quaternion iteration in a discrete time manner, the continuous time quaternion kinematics (2) can then be discretized as

$$\mathbf{q}_t = \exp\left[\frac{\Delta t}{2}\boldsymbol{\Omega}(\boldsymbol{\omega}_t)\right]\mathbf{q}_{t-1} \quad (12)$$

where  $\exp[\cdot]$  denotes the matrix exponential and the variable with subscript  $t$  stands for the corresponding value at time instant  $t$ . The notation  $\Delta t$  represents the sample period.

Under the assumption that the angular velocity remains constant over the sampling interval  $[t, t + \Delta t]$ , this exact solution incorporates all higher-order terms in  $\Delta t$  via the Taylor expansion [37]

$$\exp\left[\frac{\Delta t}{2}\boldsymbol{\Omega}(\boldsymbol{\omega}_t)\right] = \mathbf{I} + \frac{\Delta t}{2}\boldsymbol{\Omega}(\boldsymbol{\omega}_t) + \frac{\Delta t^2}{8}\boldsymbol{\Omega}^2(\boldsymbol{\omega}_t) + \mathcal{O}(\Delta t^3) \quad (13)$$

where  $\mathcal{O}(\Delta t^3)$  stands for higher order terms. In order to leverage the EKF concept, we follow the Euler method [38] to linearize the quaternion kinematics by removing the second and higher order terms, and the discrete time quaternion kinematics (2) can then be linearized as

$$\mathbf{q}_t = \mathbf{q}_{t-1} + \frac{\Delta t}{2}\boldsymbol{\Omega}(\boldsymbol{\omega}_t)\mathbf{q}_{t-1} \quad (14)$$

However, directly using Eq. (14) for quaternion propagation in filter design faces two main difficulties. On one hand, the angular rate available is the measured signal  $\boldsymbol{\omega}_{g,t}$  instead of the true one  $\boldsymbol{\omega}_t$ , and hence is corrected by the measurement noise, which directly affects the accuracy of model (14). On the other hand, the Euler approximation neglects higher-order terms and hence also imposes negative impact on the accuracy of model (14). To accommodate these two issues, we propose to modify dynamics model (14) as

$$\mathbf{q}_t = \mathbf{q}_{t-1} + \frac{\Delta t}{2}\boldsymbol{\Omega}(\boldsymbol{\omega}_{g,t})\mathbf{q}_{t-1} + \mathbf{w}_{q,t}, \quad \mathbf{w}_{q,t} \in \mathcal{N}(0, \mathbf{Q}_{q,t}) \quad (15)$$

where the process noise  $\mathbf{w}_{q,t} = \mathbf{n}_{\omega,t} + \boldsymbol{\varepsilon}_t$  with  $\mathbf{n}_{\omega,t} \sim \mathcal{N}(0, \mathbf{Q}_{\omega,t})$  being the term introduced by the gyro measurement noise and  $\boldsymbol{\varepsilon}_t \sim \mathcal{N}(0, \mathbf{Q}_{\text{int},t})$  being introduced by the Euler approximation error. Assume that the gyroscope measurement noise and the Euler method discretization error are uncorrelated, the process noise covariance of the quaternion dynamics can be determined by

$$\mathbf{Q}_{q,t} = \mathbf{Q}_{\omega,t} + \mathbf{Q}_{\text{int},t} \quad (16)$$

Based on the continuous time bias dynamics model (7), the discrete time bias propagation can be formulated as

$$\mathbf{b}_{g,t} = \mathbf{b}_{g,t-1} + \mathbf{w}_{b,t}, \quad \mathbf{w}_{b,t} \in \mathcal{N}(0, \mathbf{Q}_{b,t}) \quad (17)$$

where  $\mathbf{w}_{b,t}$  represents the process noise associated with the gyroscope bias and  $\mathbf{Q}_{b,t}$  is the corresponding covariance matrix.

Since the attitude-propagation noise and bias drift uncertainties are independent, we define the augmented process noise covariance matrix into a unified matrix as

$$\mathbf{Q}_t = \begin{bmatrix} \mathbf{Q}_{q,t} & \mathbf{0}_{4 \times 3} \\ \mathbf{0}_{3 \times 4} & \mathbf{Q}_{b,t} \end{bmatrix} \quad (18)$$

The prediction step in the proposed AEKF propagates the state estimate by

$$\mathbf{x}_t^- = \mathbf{F}_t \hat{\mathbf{x}}_{t-1} \quad (19)$$

where  $\mathbf{x}_t^-$  indicates the predicted value at the current time step, and  $\hat{\mathbf{x}}_{t-1}$  denotes the optimal estimate at the previous time step. The state transition matrix  $\mathbf{F}_t$  is given by

$$\mathbf{F}_t = \begin{bmatrix} \mathbf{A}_q(\tilde{\boldsymbol{\omega}}_t, \Delta t) & \mathbf{0}_{4 \times 3} \\ \mathbf{0}_{3 \times 4} & \mathbf{I}_3 \end{bmatrix} \quad (20)$$

where  $\tilde{\boldsymbol{\omega}}_t = \boldsymbol{\omega}_{g,t} - \hat{\mathbf{b}}_{g,t}$  is the bias corrected angular velocity, and matrix  $\mathbf{A}_q(\tilde{\boldsymbol{\omega}}_t, \Delta t)$  is determined by

$$\mathbf{A}_q(\tilde{\boldsymbol{\omega}}_t, \Delta t) = \mathbf{I}_4 + \frac{\Delta t}{2} \boldsymbol{\Omega}(\tilde{\boldsymbol{\omega}}_t) \quad (21)$$

with its full expression provided in Appendix A. The covariance matrix of the process model is predicted by

$$\mathbf{P}_t^- = \mathbf{F}_t \hat{\mathbf{P}}_{t-1} \mathbf{F}_t^T + \mathbf{Q}_t \quad (22)$$

where  $\mathbf{P}_t^-$  denotes prior estimate covariance at the current time step and  $\hat{\mathbf{P}}_{t-1}$  denotes posterior estimate covariance at the previous time step.

2) *Quaternion Update*: During the update procedure, the filter incorporates the accelerometer and magnetometer measurements to correct the predicted quaternion and covariance matrix are updated by

$$\begin{aligned} \hat{\mathbf{x}}_t &= \mathbf{x}_t^- + \mathbf{K}_t [\mathbf{z}_t - \mathbf{h}(\mathbf{x}_t^-)] \\ \hat{\mathbf{P}}_t &= \mathbf{P}_t^- - \mathbf{K}_t \mathbf{H}_t \mathbf{P}_t^- \end{aligned} \quad (23)$$

where  $\mathbf{K}_t$  denotes Kalman gain and it is calculated with the linearized model

$$\mathbf{K}_t = \mathbf{P}_t^- \mathbf{H}_t^T (\mathbf{H}_t \mathbf{P}_t^- \mathbf{H}_t^T + \mathbf{R}_t)^{-1} \quad (24)$$

where the Jacobian matrix of the measurement model is given by

$$\mathbf{H}_t = \left. \frac{\partial \mathbf{h}(\mathbf{x}_t)}{\partial \mathbf{x}} \right|_{\mathbf{x}_t = \mathbf{x}_t^-} \quad (25)$$

and the detailed definition is presented in Appendix A.

By using the quaternion estimates through inertial-magnetic sensor fusion, i.e., the first four elements of the estimated state  $\hat{\mathbf{x}}_t$ , the heading estimation can be readily extracted from Eq. (5). However, how to modeling the process noise  $\mathbf{w}_{q,t}$  to compensate for the quaternion dynamics modeling error and adjust the magnetometer measurement covariance to account for the magnetic disturbance will be the key to improve the estimation performance. These improvements will be detailed in the next two subsections.

## B. Adaptive Process Noise Characterization

In this section, the process noise model is detailed in a physics-informed manner. We model three primary sources of uncertainty: gyroscope measurement induced process noise, Euler discretization induced process noise, and bias drift. Each component is analyzed individually, and corresponding noise covariance representations are derived to construct an adaptive process noise model.

1) *Gyroscope Measurement Induced Process Noise*: Let the noise in the gyroscope measurements be  $\mathbf{v}_{\omega,t} = [v_{x,t}^\omega \ v_{y,t}^\omega \ v_{z,t}^\omega]^T$ . As the angular velocity input for the prediction step is derived from gyroscope measurements subject to stochastic errors, these uncertainties are propagated into the process noise. Therefore, incorporating  $\mathbf{v}_{\omega,t}$  into the quaternion kinematics (2) yields

$$\begin{bmatrix} \dot{q}_w \\ \dot{q}_x \\ \dot{q}_y \\ \dot{q}_z \end{bmatrix} = \frac{1}{2} \begin{bmatrix} 0 & -v_{x,t}^\omega & -v_{y,t}^\omega & -v_{z,t}^\omega \\ v_{x,t}^\omega & 0 & v_{z,t}^\omega & -v_{y,t}^\omega \\ v_{y,t}^\omega & -v_{z,t}^\omega & 0 & v_{x,t}^\omega \\ v_{z,t}^\omega & v_{y,t}^\omega & -v_{x,t}^\omega & 0 \end{bmatrix} \begin{bmatrix} q_w \\ q_x \\ q_y \\ q_z \end{bmatrix} \quad (26)$$

which presents the continuous quaternion noise caused by the gyroscope noises. Consequently, we derive a noise model by transforming the gyroscope measurement error (26) into the quaternion domain as

$$\mathbf{n}_{\omega,t} = \frac{\Delta t}{2} \boldsymbol{\Phi}(\hat{\mathbf{q}}_{t-1}) \mathbf{v}_{\omega,t} \quad (27)$$

where  $\boldsymbol{\Phi}(\hat{\mathbf{q}}_{t-1})$  is the mapping matrix that projects the 3-D angular rate uncertainties into the 4-D quaternion space, defined as

$$\boldsymbol{\Phi}(\mathbf{q}_t) = \begin{bmatrix} -q_x & -q_y & -q_z \\ q_w & -q_z & q_y \\ q_z & q_w & -q_x \\ -q_y & q_x & q_w \end{bmatrix} \quad (28)$$

The process noise covariance matrix is computed using the gyroscope measurement noise covariance

$$\mathbf{Q}_{\omega,t} = \mathbb{E} [\mathbf{n}_{\omega,t} \mathbf{n}_{\omega,t}^T] = \frac{\Delta t^2}{4} \boldsymbol{\Phi}(\hat{\mathbf{q}}_{t-1}) \boldsymbol{\Sigma}_{\omega} \boldsymbol{\Phi}^T(\hat{\mathbf{q}}_{t-1}) \quad (29)$$

where  $\mathbb{E}[\cdot]$  denotes the mathematical expectation operation.

2) *Euler Discretization Induced Process Noise*: The discrete-time approximation in Eq. (15) truncates this series by only leveraging the first-order term, thereby introducing integration errors. It is clear that the discretization error can be reduced by compensating for the higher-order terms. To balance the accuracy and computational tractability, we propose to incorporate the second-order term to mitigate the approximation error. The resulting discretization error can be expressed as the difference between the first-order and the second-order approximations, i.e.,

$$\boldsymbol{\varepsilon}_t = \frac{\Delta t^2}{8} \boldsymbol{\Omega}^2(\boldsymbol{\omega}_{g,t}) \hat{\mathbf{q}}_{t-1} \quad (30)$$

Assuming the angular velocity is isotropically distributed, the covariance matrix of the truncation error can be approximated by

$$\mathbf{Q}_{int,t} = \mathbb{E} [\boldsymbol{\varepsilon}_t \boldsymbol{\varepsilon}_t^T] \approx \frac{\Delta t^4}{64} \|\boldsymbol{\omega}_{g,t}\|^4 \hat{\mathbf{q}}_{t-1} \hat{\mathbf{q}}_{t-1}^T \quad (31)$$

3) *Gyroscope Bias Error*: In practical scenarios, gyroscope measurements are affected by slowly drifting biases. If left unmodeled, these biases accumulate over time and cause long-term drift in heading estimates [39]. To address this, we explicitly model the gyroscope bias kinematics as a random walk process, as described in Eq. (7). To derive a discrete time formulation suitable for implementation, we integrate both sides of the continuous time equation over a sampling interval  $\Delta t$  as

$$\mathbf{b}_{g,t} - \mathbf{b}_{g,t-1} = \int_{t-1}^t \dot{\mathbf{b}}_g(\tau) d\tau = \int_{t-1}^t \mathbf{v}_b(\tau) d\tau \quad (32)$$

where  $\tau$  is a dummy variable of integration over the interval  $[t-1, t]$ . According to Eq. (17), the discrete time noise term  $\mathbf{w}_{b,t}$  can be expressed as

$$\mathbf{w}_{b,t} = \int_{t-1}^t \mathbf{v}_b(\tau) d\tau \quad (33)$$

Under the white noise assumption,  $\mathbf{w}_{b,t}$  remains zero-mean Gaussian, and its covariance is given by

$$\begin{aligned} \mathbf{Q}_{b,t} &= \mathbf{E}[\mathbf{w}_{b,t} \mathbf{w}_{b,t}^T] = \int_{t-1}^t \int_{t-1}^t \mathbf{E}[\mathbf{v}_b(\tau) \mathbf{v}_b^T(\sigma)] d\tau d\sigma \\ &= \int_{t-1}^t \int_{t-1}^t \Sigma_b \delta(\tau - \sigma) d\tau d\sigma \\ &= \Sigma_b \Delta t \end{aligned} \quad (34)$$

where  $\sigma$  is a dummy variable and  $\delta(\cdot)$  is the Dirac delta function.

### C. Adaptive Magnetometer Measurement Noise Covariance

In indoor environments with cluttered electronic equipment and metallic objects, magnetometer measurements are often degraded by strong magnetic disturbances. It is important to note that our approach builds upon a one-time, offline calibration performed prior to deployment. This initial calibration compensates for sensor-intrinsic hard and soft iron biases and establishes the local reference magnetic field vector. The adaptive mechanism detailed in this section is specifically designed to handle external, time-varying disturbances encountered during operation. The core idea of this strategy is to compute the deviation between the measured magnetic field vector in the body frame and the predicted magnetic field based on the current state estimate. This deviation, denoted as  $\delta_m$ , is calculated by

$$\delta_m = \|\mathbf{y}_{m,t} - \mathbf{h}_{mag}(\mathbf{q}_t^-)\| \quad (35)$$

where  $\mathbf{h}_{mag}(\mathbf{q}_t^-)$  is the predicted magnetic field vector derived from the current quaternion estimate. We employ a Chi-square distribution [40] based on the magnetometer measurement residual  $\delta_m$  to establish a criterion for detecting disturbances. Under nominal conditions, the squared Mahalanobis distance of the residual is defined as

$$d^2 = \delta_m^T \mathbf{R}_m^{-1} \delta_m \quad (36)$$

which follows a Chi-square distribution with three degrees of freedom, denoted as

$$d^2 \sim \chi_3^2, \quad P(d^2 \leq \chi_{3,p_i}^2) = p_i, \quad i = 1, 2 \quad (37)$$

where  $p_i$  represents predefined confidence levels associated with disturbance severities. Accordingly, thresholds  $\tau_1$  and  $\tau_2$  are determined by

$$\tau_i = \sigma_m \sqrt{\chi_{3,p_i}^2}, \quad i = 1, 2 \quad (38)$$

where  $\sigma_m = \sqrt{\frac{\text{trace}(\mathbf{R}_m)}{3}}$  is the standard deviation of magnetometer measurement noise under nominal conditions. The adaptive mechanism identifies disturbances by comparing the magnetometer innovation residual  $\delta_m$  against predefined thresholds,  $\tau_1$  and  $\tau_2$ . These thresholds are derived from the chi-squared distribution, corresponding to confidence levels of  $p_1 = 0.95$  for severe disturbances and  $p_2 = 0.35$  for moderate ones, respectively. Based on these levels, a piecewise function scales the magnetometer noise covariance  $\mathbf{R}_m$  as follows

$$\mathbf{R}_m = \begin{cases} \lambda_1 \mathbf{R}_m, & \text{if } \delta_m > \tau_1 \quad (\text{severe disturbance}) \\ \lambda_2 \mathbf{R}_m, & \text{if } \tau_2 < \delta_m \leq \tau_1 \quad (\text{moderate disturbance}) \\ \mathbf{R}_m, & \text{otherwise} \quad (\text{nominal conditions}) \end{cases} \quad (39)$$

The disturbance scaling coefficients,  $\lambda_1$  and  $\lambda_2$ , are empirically tuned using a validation dataset collected within the same indoor environment where the subsequent experiments are conducted. Specifically,  $\lambda_1$  is a large factor chosen to aggressively inflate the measurement covariance during severe disturbances, effectively causing the filter to reject the corrupted measurement. In contrast,  $\lambda_2$  is a more moderate factor used to down-weight the magnetometer's influence during transient disturbances. The confidence levels  $p_1$  and  $p_2$  can also be tuned to adapt the filter to different platforms and operational environments. For UAVs operating in magnetically challenging conditions, a more conservative tuning is recommended to prioritize robustness. This is achieved by lowering both  $p_1$  and  $p_2$  to make the filter more sensitive to anomalies. Conversely, for platforms in relatively clean environments, accuracy can be maximized by raising  $p_2$  to trust the magnetometer more frequently, while keeping  $p_1$  high to ensure only genuinely extreme outliers are rejected. This adaptive strategy ensures the robustness and accuracy of the heading estimation by dynamically adjusting the magnetometer's credibility to compensate for varying magnetic conditions in complex indoor environments.

## V. NONLINEAR OBSERVABILITY ANALYSIS

In order to assess whether the heading angle can be estimated by the filter, we perform a nonlinear observability analysis. A nonlinear system is locally observable if the rank of the observability matrix  $\Xi$  equals the dimension of the state, i.e.,  $\text{rank}(\Xi) = \dim(\mathbf{x})$ . Following the methods presented in [41], an observability matrix derived from Lie derivatives is established. For the general definition, the observability matrix is constructed by stacking the gradients of successive Lie derivatives as

$$\Xi = \begin{bmatrix} \nabla_{\mathbf{x}} \mathcal{L}^0 \mathbf{h}(\mathbf{q}) \\ \nabla_{\mathbf{x}} \mathcal{L}^1 \mathbf{h}(\mathbf{q}) \\ \vdots \\ \nabla_{\mathbf{x}} \mathcal{L}^k \mathbf{h}(\mathbf{q}) \end{bmatrix}, \quad k \leq n-1 \quad (40)$$

where

$$\begin{aligned}\mathcal{L}^0 \mathbf{h}(\mathbf{q}) &= \mathbf{h}(\mathbf{q}) \\ \mathcal{L}_f^k \mathbf{h}(\mathbf{q}) &= \frac{\partial \mathcal{L}_f^{k-1} \mathbf{h}(\mathbf{q})}{\partial \mathbf{x}} \mathbf{f}(\mathbf{x}) \\ \nabla_{\mathbf{x}} \mathcal{L}_f^k \mathbf{h}(\mathbf{q}) &= \frac{\partial \mathcal{L}_f^k \mathbf{h}(\mathbf{q})}{\partial \mathbf{x}}\end{aligned}\quad (41)$$

and  $\nabla_{\mathbf{x}}(\cdot)$  denotes the gradient of  $(\cdot)$  with respect to  $\mathbf{x}$  and  $n$  is the dimension of the state  $\mathbf{x}$ . In this formulation, the superscript  $n - 1$  denotes that Lie derivatives are computed up to the  $n - 1$  order to construct  $n$  linearly independent gradient terms for an  $n$ -dimensional state vector. In our specific case, considering the zeroth and first order Lie derivatives is sufficient to show that the observability matrix attains full rank, which is equal to the dimension of the state  $\mathbf{x}$ , i.e., the observability matrix can be established as

$$\Xi = \begin{bmatrix} \nabla_{\mathbf{x}} \mathcal{L}^0 \mathbf{h}(\mathbf{q}) \\ \nabla_{\mathbf{x}} \mathcal{L}_f^1 \mathbf{h}(\mathbf{q}) \end{bmatrix} \in \mathbb{R}^{12 \times 7} \quad (42)$$

Then, the observability of the proposed filter is presented in the following proposition, which indicates the system state, including the quaternion and bias, is locally observable, theoretically guaranteeing the convergence of the filter developed.

**Proposition 1.** *The rank of the observability matrix  $\Xi$  associated with the proposed AMO-HEAD equals the dimension of the system state, i.e.,  $\text{rank}(\Xi) = 7$ .*

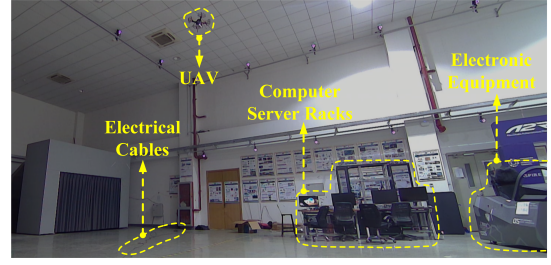
**Proof.** A rigorous proof of the full rank property is presented in the Appendix B. ■

## VI. EXPERIMENTS VALIDATION

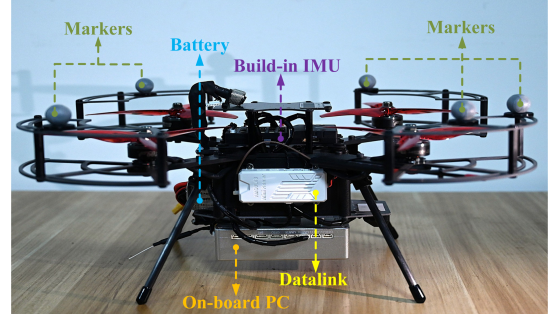
In this section, we present a set of experiments in indoor environments subject to magnetic disturbances, as shown in Fig. 3a. These experiments demonstrate the effectiveness and robustness of the proposed AEKF-based heading estimation algorithm. We first describe the equipment setup and the specific UAV hardware platform. Next, we discuss the indoor magnetic environment and demonstrate how significant field disturbances affect raw magnetometer readings. Then we conduct comparative experiments using four progressively refined designs of our algorithm: (1) EKF-4D: using only a 4-dimensional quaternion as state variables with random-walk process noise; (2) EKF-7D: expanding the state to 7 dimensions by incorporating gyroscope biases, still with random-walk noise; (3) EKF-Accurate: implementing refined modeling of process noise in addition to the 7-dimensional state; and (4) AMO-HEAD: further adding an adaptive measurement noise covariance module to the refined model in case (3). In addition, we compare the proposed method with several representative open-source heading estimation algorithms to benchmark its performance under magnetically disturbed conditions.

### A. Equipment Setup

Our experiments were conducted on a customized quadrotor UAV shown in Fig. 3b. It is equipped with a Jetson Orin NX on-board computer featuring 2.0 GHz Arm Cortex-A7 CPU and 16 GB RAM. The computer runs Ubuntu 20.04 with the



(a) The indoor inspection area is filled with server racks and electronic equipment, resulting in magnetic disturbances



(b) Our quadrotor platform with hardware details for data acquisition. The quadrotor is tested within a motion capture system

Fig. 3: Experimental settings.

Robot Operating System (ROS) middleware for sensor data handling and real-time control. The UAV's flight controller integrates an IMU containing three-axis accelerometers and gyroscopes, as well as a dedicated three-axis magnetometer for heading measurements.

To obtain ground truth pose information for validation, we employed a motion capture system composed of 44 cameras arranged in two layers: an upper layer of 24 cameras approximately 6 m above the ground, and a lower layer of 20 cameras situated around 3 m high, as shown in Fig. 3a. Covering a measurement volume of  $17 \text{ m} \times 17 \text{ m} \times 5 \text{ m}$ , the system delivers centimeter-level positioning precision throughout this space and maintains sub-degree angular accuracy, making it well-suited for reliably capturing the UAV's position and orientation in real time. In the following experiments, the motion capture system provides the reference heading as ground truth.

### B. Magnetic Field Conditions and Disturbance Effects

Our tests were performed in a lab containing electrical equipment and steel structures. To quantitatively characterize this magnetically cluttered environment, we compute the magnetic field magnitude  $\mathbf{B}$  over the experimental duration with

$$|\mathbf{B}| = \sqrt{y_{mx}^2 + y_{my}^2 + y_{mz}^2} \quad (43)$$

which is shown in Fig. 4. The summary statistics show a mean magnetic field magnitude  $\mu_{|\mathbf{B}|}$  of  $45.83 \mu\text{T}$ , with a standard deviation  $\sigma_{|\mathbf{B}|}$  of  $11.13 \mu\text{T}$ . The coefficient of variation

$$C_v = \frac{\sigma_{|\mathbf{B}|}}{\mu_{|\mathbf{B}|}} \quad (44)$$

gives a value of 24.28%, which markedly exceeds the 10% threshold used to assess significant magnetic deviation [42].

Thus, it indicates the pronounced magnetic disturbance. In addition, the peak magnitude reaches  $127.34 \mu T$ , approximately  $2.78\times$  the mean value, further corroborating the presence of strong local disturbance sources. These local magnetic field distortions noticeably affect the raw three-axis magnetometer readings. As the UAV should rotate to

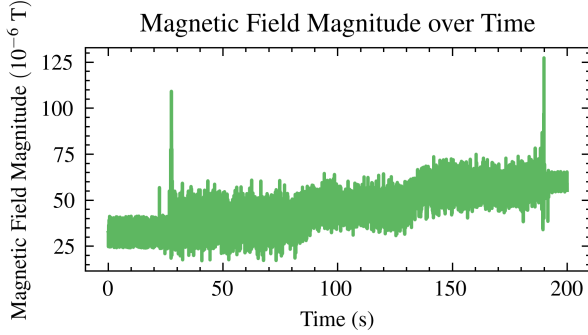


Fig. 4: Magnetic field magnitude recorded in the experimental environment.

scan its surroundings in order to fully cover the inspection area, we consider the scenario that involves a UAV hovering approximately 6 m high, changing its heading angle without translating. Specifically, the UAV hovers steadily at a fixed altitude in indoor environment while performing controlled heading rotations. The heading angle transitions from  $2.8^\circ$  to  $95.8^\circ$ , and then to  $186.5^\circ$  by a human pilot, with the UAV holding each orientation for a defined duration. Specifically, the UAV undergoes three distinct phases: in the first phase it maintains a heading of  $2.8^\circ$  for 70 seconds, in the second phase  $95.8^\circ$  for 50 seconds, and in the third phase  $186.5^\circ$  for another 50 seconds.

The magnetometer readings in this scenario, shown in Fig. 5, demonstrate significant variability. At  $T = 20s$ , sudden magnetic anomalies are observed on both the Y and Z axes. The Y-axis abruptly spikes to  $60\mu T$ , and the Z-axis jumps sharply to  $-100\mu T$ . Later at  $T = 180s$ , the Z-axis value increases to  $-120\mu T$ , exceeding the typical Earth's magnetic field magnitude [43]. These pronounced magnetic field disturbances captured by the magnetometer readings indicate the nature of the laboratory's magnetic environment. Such interferences confirm the necessity of adopting a robust sensor-fusion strategy instead of solely relying on the raw outputs for heading calculations.

Figure 6 compares the heading angle directly computed from raw magnetometer readings with the ground truth obtained from the motion capture system. During the first phase, the magnetometer-derived heading shows significant deviation from the ground truth, with errors reaching several tens of degrees at peak disturbance points. During the transition from first phase to second phase, the magnetometer output lags behind the actual UAV rotation, failing to accurately track the change in heading. In the second phase, a noticeable constant bias persists between the magnetometer-based heading and the ground truth. These results demonstrate that relying solely on magnetometer for heading estimation can lead to severe

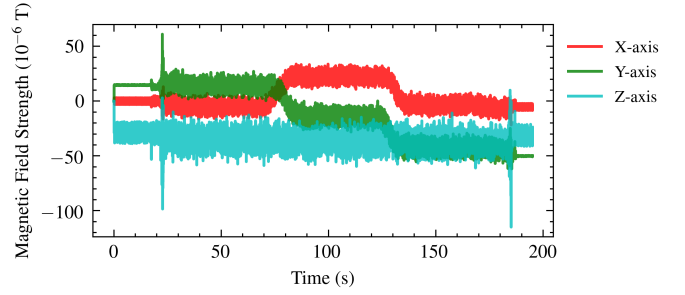


Fig. 5: MARG sensor raw data collected in the experimental environment.

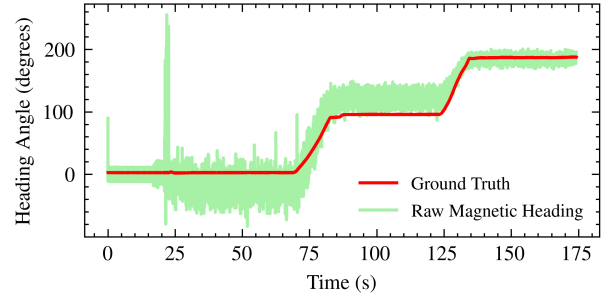


Fig. 6: Comparison between UAV heading angles computed from disturbed raw magnetometer readings and ground truth headings provided by the motion capture system.

instability in UAV orientation, potentially posing risks during inspection tasks.

### C. Heading Estimation Accuracy Evaluation

To validate the performance of the proposed AMO-HEAD approach, we conducted comparative tests of the progressively refined algorithm variants. The filter is initialized with state  $\mathbf{x}_0 = [1, 0, 0, 0, 0, 0, 0]^T$ , representing a nominal unit quaternion and zero gyroscope bias, and with initial estimation error covariance  $\mathbf{P}_0 = 0.1 \mathbf{I}_7$ . The process noise covariance is initialized as  $\mathbf{Q}_0 = \text{diag}(0.02, 0.02, 0.02, 0.02, 10^{-6}, 10^{-6}, 10^{-6})$ . The initial acceleration measurement noise covariance is set to  $\mathbf{R}_a = \text{diag}(0.01, 0.01, 0.01)$  and magnetometer measurement noise covariance is set to  $\mathbf{R}_m = \text{diag}(0.1, 0.1, 0.1)$ . The local reference magnetic field is set to  $\mathbf{m} = [-2.81, 14.67, -28.64]^T$  in the inertial frame. Four algorithm variants use the same initial values and the estimation results compared with the ground truth heading are presented in Fig. 7. From the initial stage, it can be seen that the proposed AMO-HEAD have faster convergence efficiency compared to three other variants. In the first and third phase with severe magnetic disturbances, the EKF-4D algorithm demonstrates the largest deviations from the ground truth, exhibiting slow convergence. For the EKF-7D variant, the estimation follows a similar overall trend to EKF-4D but shows improved alignment with the true heading. However, noticeable overshoot occurs at  $T = 70s$ , and substantial deviations remain around the second phase, accompanied by slow convergence. The EKF-Accurate algorithm, benefiting from detailed process noise modeling, achieves

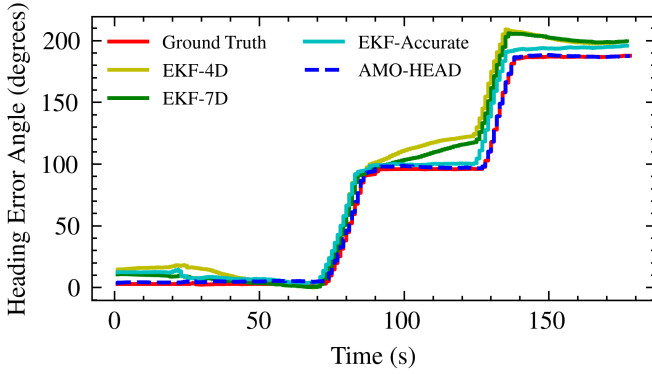


Fig. 7: Comparison of four progressively refined heading estimation results with ground truth in the UAV self-rotation scenario.

improved convergence at the second phase, yielding estimates generally close to the ground truth, although convergence at the first phase is slow. Finally, the proposed AMO-HEAD approach, indicated by the blue dashed curve, demonstrates superior accuracy with rapid convergence and close alignment to the ground truth across all phases. It clearly highlights its robust estimation in mitigating magnetic disturbances via adaptive covariance scaling.

To further quantify performance, we compare each heading estimate to the ground truth heading from the motion capture system and calculate the error. Specifically, we compute the heading difference through

$$e_i(t) = \hat{\psi}_i(t) - \psi_{GT}(t), \quad (45)$$

where  $\hat{\psi}_i(t)$  is the heading estimate from method  $i \in \{\text{EKF-4D}, \text{EKF-7D}, \text{EKF-Accurate}, \text{AMO-HEAD}\}$  at time  $t$ , and  $\psi_{GT}(t)$  is the corresponding ground truth heading. The errors

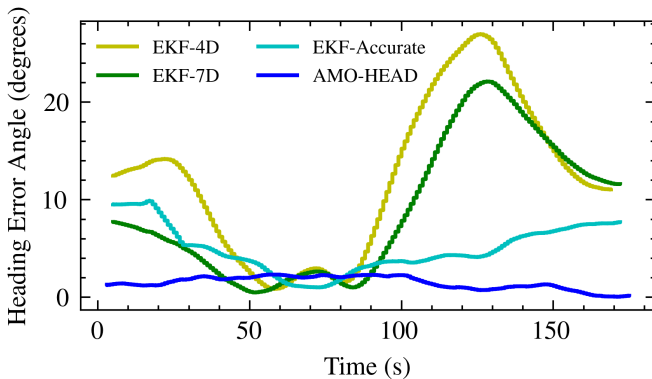


Fig. 8: Estimation errors of four progressively refined algorithms in the UAV self-rotation scenario.

are shown in Fig. 8. For the EKF-4D and EKF-7D methods, the heading estimation errors exhibit significant instability, with sudden jumps ranging from  $4^\circ$  to  $30^\circ$ . During approximately half of the experimental duration, the heading errors surpass  $10^\circ$ , presenting substantial risks to UAV stability and safe inspection tasks. Overall, EKF-Accurate demonstrates

TABLE I: Error Metrics of the Refined Estimation Algorithm

Method	EKF-4D	EKF-7D	EKF-Accurate	AMO-HEAD
RMSE	$14.55^\circ$	$11.91^\circ$	$6.26^\circ$	$1.58^\circ$
MAE	$12.15^\circ$	$10.07^\circ$	$6.01^\circ$	$1.42^\circ$

noticeably smaller errors compared to the previous two methods. However, during the periods of substantial magnetic disturbances at first and third phases, it still produces errors of around  $8^\circ$  to  $10^\circ$ , revealing its limited capability to resist severe magnetic interference. In contrast, the proposed AMO-HEAD consistently maintains low error levels around  $2^\circ$  throughout the experiment. Remarkably, its estimation error approaches zero for nearly half of the testing period, confirming exceptionally accurate and stable heading estimation performance. To evaluate the overall accuracy of each heading estimation approach, we also calculate the root mean squared error (RMSE) and mean absolute error (MAE) of the heading outputs over the full experimental sequence and show the results in Table I. The RMSE is defined as

$$\text{RMSE} = \sqrt{\frac{1}{N} \sum_{i=1}^N (\hat{\psi}_i - \psi_{GT})^2} \quad (46)$$

and measures the square-root of the average squared deviation between the estimated heading and the ground truth. The MAE is given by

$$\text{MAE} = \frac{1}{N} \sum_{i=1}^N |\hat{\psi}_i - \psi_{GT}| \quad (47)$$

and quantifies the average absolute deviation. Here,  $N$  is the total number of samples in the experimental sequence. These two complementary metrics together provide an assessment of estimation error. Consistent with the previously discussed heading estimation curves in Fig. 7, the EKF-7D method slightly outperforms EKF-4D, reducing RMSE by  $2.64^\circ$ , and lowering MAE from  $12.15^\circ$  to  $10.07^\circ$ . The EKF-Accurate method significantly surpasses EKF-7D, achieving a 47.4% reduction in RMSE and a corresponding MAE decrease to  $6.01^\circ$ . Finally, benefiting from refined process noise modeling and the adaptive measurement noise covariance scaling module, AMO-HEAD attains exceptionally low error values. It achieves an RMSE of only  $1.58^\circ$  and an MAE of  $1.42^\circ$ , notably falling below  $2^\circ$ .

#### D. Comparison with Open-Source Estimation Algorithms

To further evaluate the proposed AMO-HEAD approach, we conducted comparative experiments against three state-of-the-art (SOTA) heading estimation methods: VQF [42], KOK [11], and QMT [44]. This selection provides a comprehensive benchmark, as each algorithm represents a distinct and significant strength in the field. VQF serves as the primary high-accuracy benchmark. It has demonstrated superior performance in the extensive evaluations and has been validated with excellent results on UAV datasets. KOK, also recognized as a SOTA method in the VQF study, is

included for its notable robustness against short-term magnetic field disturbances. Finally, QMT is chosen for its exceptional computational efficiency, offering one of the fastest implementations while maintaining strong accuracy. Specifically, in the

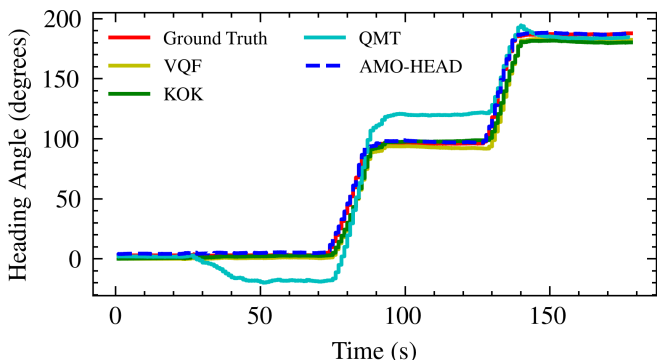


Fig. 9: Comparison of heading estimates from the proposed AMO-HEAD approach and three open-source methods against the ground truth trajectory during UAV self-rotation.

VQF framework, strapdown gyroscope integration propagates an orientation quaternion to capture high frequency angular motion. A gravity-referenced tilt correction quaternion then removes roll and pitch drift using accelerometer data, and a scalar yaw adjustment accumulates magnetometer-derived heading corrections. The initial attitude state is defined by setting both the gyroscope-integrated quaternion and the gravity-corrected quaternion to the identity quaternion  $[1, 0, 0, 0]^T$  and initializing the magnetometer-derived yaw correction angle to  $0^\circ$ . The KOK method parameterizes orientation corrections as a minimal 3D rotation increment and applying a single fixed step gradient descent update to reduce computational load. The algorithm maintains two coupled state variables, an orientation quaternion  $\mathbf{q}$  and a 3-D gyroscope bias  $\mathbf{b}_g$ , which are initialized to  $[1, 0, 0, 0]^T$  and  $[0, 0, 0]^T$ , respectively. For QMT, it is a quaternion-based inertial motion tracking toolbox and we run the `oriEstIMU` algorithm in the toolbox. At each sampling interval, the bias-corrected angular rate is strapdown integrated to produce a predicted quaternion. Then it is refined by an accelerometer-based tilt correction and a magnetometer-based yaw correction. The initial state vector of QMT is same as KOK.

Importantly, these three methods rely solely on MARG sensor measurements as inputs and are processed with identical dataset collected from the experiment, allowing direct comparison against the ground truth. Figure 9 illustrates the heading angle estimations produced by each algorithm. Notably, the QMT algorithm displays obvious deviations and instability in the middle phase of the dataset. VQF and KOK follow the true heading reasonably well but still show noticeable errors, while AMO-HEAD stays closest to the ground truth trajectory. This demonstrates the robustness and accuracy of the proposed algorithm under challenging magnetic conditions. Quantitative results presented in Fig. 10 further reinforce these observations. AMO-HEAD achieves the lowest RMSE and MAE of all tested methods, with errors far below those of the three open-source benchmark algorithms. QMT shows

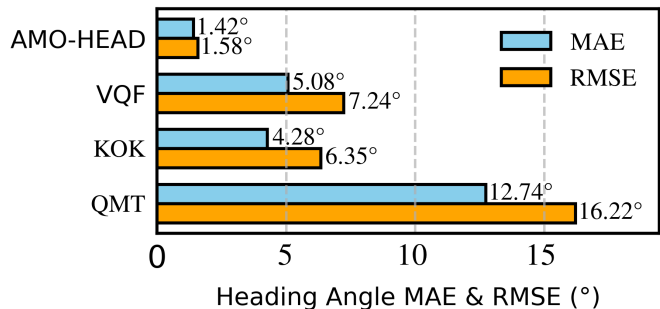


Fig. 10: Heading estimation performance of the proposed AMO-HEAD and three open-source algorithms. Blue bars denote MAE and orange bars denote RMSE, with values in degrees.

TABLE II: Runtime Comparison of AMO-HEAD and Three Baseline Algorithms

Method	AMO-HEAD	VQF	QMT	KOK
Single-step (ms)	0.162	0.223	0.190	1.943
Per-step (ms)	0.260	0.354	0.242	2.572

the largest errors throughout the sequence. VQF updates its gyroscope bias only during detected stationary intervals. When a magnetometer reading is flagged as an outlier, the filter directly skips the magnetic correction step to reject that disturbance. In comparison, AMO-HEAD’s refined noise model is a fully continuous, data-driven adjustment that tracks gyro noise characteristics at all times. Meanwhile, AMO-HEAD avoids hard ‘all-or-nothing’ cutoffs that lose potentially valuable information during moderate disturbances. AMO-HEAD automatically adapts its tuning to the varying disturbance levels. The results validate that the proposed algorithm is a reliable and robust solution for real world UAV heading estimation tasks.

Quantitative runtime evaluation further complements the accuracy evaluation. To substantiate the lightweight design, we perform a runtime comparison on a laptop with 2.20 GHz Intel Core i7 CPU and 16 GB RAM. All four methods are wrapped under a unified ROS interface, and we instrument the core filter step to measure execution time. We have two metrics for the evaluation, the minimum single-step runtime and the average per-step runtime over the entire dataset. The results are summarized in Table II. AMO-HEAD achieves the fastest single-step runtime of 0.162 ms, outperforming VQF and QMT. In terms of average runtime, AMO-HEAD performs comparably to the fastest baseline QMT, with a difference of less than 0.02 ms. The KOK baseline, whose open-source implementation is MATLAB-based, exhibits obvious higher runtimes. These results highlight that AMO-HEAD not only achieves superior accuracy but also maintains computational efficiency suitable for real-time UAV deployment.

#### E. Long-Term Performance and Generalizability Validation

To validate the long-term stability and generalizability of our approach, we conduct an additional experiment designed

TABLE III: Error Metrics of the Long-Term Experiment

Method	AMO-HEAD	VQF	QMT	KOK
RMSE	6.16°	11.72°	8.61°	11.22°
MAE	4.62°	9.74°	7.15°	8.35°

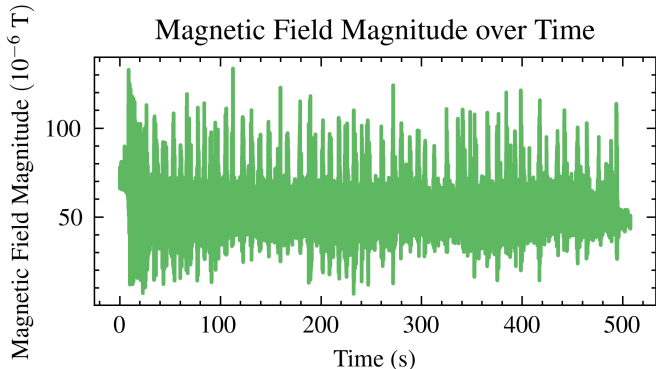


Fig. 11: Magnetic field magnitude recorded during the 8-minute flight. The high volatility and sharp peaks indicate a magnetically challenging environment with strong, structured interference.

to test AMO-HEAD’s robustness against accumulated drift and its performance in a distinct operational environment. The experiment is consisted of a continuous, manually-piloted flight of approximately 8 minutes, with the duration limited by the UAV’s battery endurance. We perform this test in an indoor area populated with electronic hardware and metallic infrastructure. As illustrated in Fig. 11, this environment is characterized by strong, structured magnetic interference, with transient peak disturbances. The UAV follows a repetitive square trajectory, involving segments of straight-line motion followed by 90-degree heading turns. A motion capture system provides high-fidelity ground truth for the entire flight.

We benchmark the performance of AMO-HEAD against the same open-source methods. The heading estimation results are illustrated in Fig. 12. It is visually evident that AMO-HEAD remains consistently aligned with the ground truth, accurately tracking the repetitive turns without accumulating noticeable drift. In contrast, the other methods exhibit larger tracking errors and intermittent drift, with particularly significant deviations occurring during and after the sharp heading maneuvers.

Quantitative analysis, summarized in Table III, further substantiates these findings. AMO-HEAD achieves an RMSE of 6.16° and an MAE of 4.62°, significantly outperforming all other methods. This result demonstrates two key strengths of our approach. First, the robust gyroscope bias estimation effectively prevents long-term drift, ensuring stable performance over long-duration missions. Second, the successful performance in a new, challenging environment confirms the generalizability of our adaptive framework, which automatically adjusts its sensor fusion strategy to match the ambient magnetic conditions.

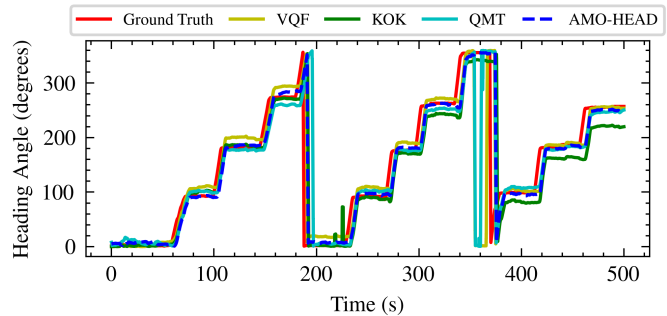


Fig. 12: Comparison of heading estimates over the 8-minute long-term trajectory. AMO-HEAD demonstrates superior stability and tracking accuracy, closely following the ground truth without accumulating drift, unlike the benchmark algorithms.

## VII. CONCLUSION

In this paper, we formulate a MARG-only quaternion-based AEKF framework that advances UAV heading estimation, with incorporating gyroscope biases into the state vector. We introduce a refined process noise model that considers gyroscope measurement errors, slow bias drifts, and discretization errors induced by the integration using Euler method. Moreover, an adaptive measurement noise covariance matrix is implemented to suppress magnetic disturbances indoors. Furthermore, observability of the proposed model is proven using Lie derivative analysis. Additionally, our framework offers a computationally efficient implementation, achieving real-time performance on ARM Cortex-A7 processors. Experimental validation under severe indoor magnetic disturbances demonstrates a heading estimation RMSE of 1.58°, outperforming all the evaluated benchmark algorithms. Together, this comprehensive framework establishes a reliable model for resource-constrained aerial autonomy in indoor inspection tasks. Furthermore, the core adaptive mechanism of our framework demonstrates significant potential for generalization. Its principle of dynamically weighting measurements offers a more robust solution than rigid rejection logic. It also provides a cost-effective alternative to expensive hardware, addressing common limitations found on other platforms such as ground and underwater vehicles. This makes our approach a promising candidate for robust heading estimation across the field of robotics.

## APPENDIX A

### BACKGROUND DEFINITIONS AND MATRIX FORMULATIONS

This appendix provides supplementary definitions and matrix formulations referenced in the main text. Specifically, we first define the coordinate systems used throughout the paper. We then present the full expressions for the key matrices in our AEKF-based framework: the quaternion-to-rotation matrix  $\mathbf{C}(\mathbf{q})$ , the state transition sub-matrix  $\mathbf{A}_q$ , and the measurement Jacobian matrix  $\mathbf{H}_t$ .

#### A. Coordinate Frame Definitions

This work employs two primary coordinate systems: an inertial frame and a body frame. The inertial frame  $\{n\}$

$$\mathbf{H}_t = \begin{bmatrix} -2gq_y & 2gq_z & -2gq_w & 2gq_x & 0 & 0 & 0 \\ 2gq_x & 2gq_w & 2gq_z & 2gq_y & 0 & 0 & 0 \\ 2gq_w & -2gq_x & -2gq_y & 2gq_z & 0 & 0 & 0 \\ 2m_x^r q_w + 2m_z^r q_y & 2m_x^r q_x + 2m_z^r q_z & -2m_x^r q_y + 2m_z^r q_w & -2m_x^r q_z + 2m_z^r q_x & 0 & 0 & 0 \\ 2m_x^r q_z - 2m_z^r q_x & 2m_x^r q_y - 2m_z^r q_w & 2m_x^r q_x + 2m_z^r q_z & 2m_x^r q_w + 2m_z^r q_y & 0 & 0 & 0 \\ -2m_x^r q_y + 2m_z^r q_w & 2m_x^r q_z - 2m_z^r q_x & -2m_x^r q_w - 2m_z^r q_y & 2m_x^r q_x + 2m_z^r q_z & 0 & 0 & 0 \end{bmatrix} \quad (50)$$

follows the east-north-up (ENU) convention, where its axes point towards east ( $\mathbf{e}_E$ ), north ( $\mathbf{e}_N$ ), and up ( $\mathbf{e}_U$ ), respectively. The body frame  $\{b\}$  is rigidly attached to the UAV's airframe. The MARG sensor module is mounted such that its axes align with the UAV's forward, left, and upward directions. Consequently, the sensor frame axes and body frame axes ( $\mathbf{e}_x$ ,  $\mathbf{e}_y$ ,  $\mathbf{e}_z$ ) are coincident, allowing any vector expressed in the sensor frame to be directly used in the body frame without additional transformation.

### B. Filter Matrix Formulations

First, the rotation matrix  $\mathbf{C}(\mathbf{q})$ , which transforms a vector from the inertial frame  $\{n\}$  to the body frame  $\{b\}$ , is formulated from the unit quaternion  $\mathbf{q}$  as follows

$$\mathbf{C}(\mathbf{q}) = \begin{bmatrix} q_w^2 + q_x^2 - q_y^2 - q_z^2 & 2(q_x q_y + q_w q_z) & 2(q_x q_z - q_w q_y) \\ 2(q_x q_y - q_w q_z) & q_w^2 - q_x^2 + q_y^2 - q_z^2 & 2(q_y q_z + q_w q_x) \\ 2(q_x q_z + q_w q_y) & 2(q_y q_z - q_w q_x) & q_w^2 - q_x^2 - q_y^2 + q_z^2 \end{bmatrix} \quad (48)$$

Next, the state transition sub-matrix for the quaternion kinematics,  $\mathbf{A}_q(\tilde{\omega}_t, \Delta t)$ , derived via a first-order Euler approximation, is defined as

$$\begin{aligned} \mathbf{A}_q(\tilde{\omega}_t, \Delta t) &= \mathbf{I}_4 + \frac{\Delta t}{2} \boldsymbol{\Omega}(\tilde{\omega}_t) \\ &= \begin{bmatrix} 1 & -\frac{\Delta t}{2} \tilde{\omega}_x & -\frac{\Delta t}{2} \tilde{\omega}_y & -\frac{\Delta t}{2} \tilde{\omega}_z \\ \frac{\Delta t}{2} \tilde{\omega}_x & 1 & \frac{\Delta t}{2} \tilde{\omega}_z & -\frac{\Delta t}{2} \tilde{\omega}_y \\ \frac{\Delta t}{2} \tilde{\omega}_y & -\frac{\Delta t}{2} \tilde{\omega}_z & 1 & \frac{\Delta t}{2} \tilde{\omega}_x \\ \frac{\Delta t}{2} \tilde{\omega}_z & \frac{\Delta t}{2} \tilde{\omega}_y & -\frac{\Delta t}{2} \tilde{\omega}_x & 1 \end{bmatrix} \end{aligned} \quad (49)$$

Finally, the full expression for the measurement Jacobian matrix  $\mathbf{H}_t$ , evaluated at the prior state estimate  $\mathbf{x}_t^-$ , is given in Eq. (50) at the top of the next page. The first three rows of  $\mathbf{H}_t$  are the partial derivatives with respect to the accelerometer model, while the last three rows are with respect to the magnetometer model.

### APPENDIX B PROOF OF PROPOSITION 1

To enhance clarity, we first outline the high-level overview. We begin by assuming that the system operates under nonsingular attitude conditions. Singular attitudes in this study refer to configurations where the UAV roll angle  $\phi$  or pitch angle  $\theta$  equals  $\pm 90^\circ$ . We first select the  $7 \times 7$  submatrix  $\mathbf{M}$  from the complete observability matrix. Under the nonsingular-attitude assumption, we examine two alternative row combinations of  $\mathbf{A}$  and show that its determinant is nonzero across all nonsingular attitude configurations. We then prove, by contradiction,

that the determinant of  $\mathbf{B}$  never vanishes. Finally, leveraging the determinant property of block matrices, we establish that the entire submatrix  $\mathbf{M}$  is full rank, thereby confirming the system's local observability. The proof of Proposition 1 will be presented by the following four sequential steps.

1) *Submatrix Selection and Decomposition:* Based on the rank minor theorem [45], the rank of a matrix is determined by the size of its largest nonzero minor, i.e., the  $12 \times 7$  dimension of  $\boldsymbol{\Xi}$  implies that its maximum possible nonzero minor is of size  $7 \times 7$ . A selected  $7 \times 7$  minor which has a nonzero determinant would establish linear independence among its rows. To demonstrate the rank property, we select a  $7 \times 7$  submatrix  $\mathbf{M}$  of  $\boldsymbol{\Xi}$  by choosing rows  $\{1,2,3,4,7,8,9\}$  and columns  $\{1,2,3,4,5,6,7\}$ , denoted as

$$\mathbf{M} = \begin{bmatrix} \mathbf{A} & \mathbf{0} \\ \mathbf{C} & \mathbf{B} \end{bmatrix} \quad (51)$$

where

$$\begin{aligned} \mathbf{A} &= \begin{bmatrix} -2gq_y & 2gq_z & -2gq_w & 2gq_x \\ 2gq_x & 2gq_w & 2gq_z & 2gq_y \\ 2gq_w & -2gq_x & -2gq_y & 2gq_z \\ \Xi_{4,1} & \Xi_{4,2} & \Xi_{4,3} & \Xi_{4,4} \end{bmatrix} \\ \mathbf{B} &= \begin{bmatrix} 0 & \Xi_{7,6} & \Xi_{7,7} \\ \Xi_{8,5} & 0 & \Xi_{8,7} \\ \Xi_{9,5} & \Xi_{9,6} & 0 \end{bmatrix} \\ \mathbf{C} &= \begin{bmatrix} \Xi_{7,1} & \Xi_{7,2} & \Xi_{7,3} & \Xi_{7,4} \\ \Xi_{8,1} & \Xi_{8,2} & \Xi_{8,3} & \Xi_{8,4} \\ \Xi_{9,1} & \Xi_{9,2} & \Xi_{9,3} & \Xi_{9,4} \end{bmatrix} \end{aligned} \quad (52)$$

where  $\Xi_{i,j}$  denotes the  $i$ -th row and  $j$ -th column elements of the observability matrix  $\boldsymbol{\Xi}$  and the required elements in the selected submatrix can be readily obtained by some tedious but straightforward mathematical derivations as

$$\begin{cases} \Xi_{4,1} = 2q_w - q_y \\ \Xi_{4,2} = 2q_x + q_z \\ \Xi_{4,3} = -2q_y - q_w \\ \Xi_{4,4} = -2q_z + q_x \end{cases} \quad \begin{cases} \Xi_{7,1} = -2g(\tilde{\omega}_y q_w - \tilde{\omega}_z q_x) \\ \Xi_{7,2} = 2g(\tilde{\omega}_z q_w + \tilde{\omega}_y q_x) \\ \Xi_{7,3} = 2g(\tilde{\omega}_y q_y + \tilde{\omega}_z q_z) \\ \Xi_{7,4} = 2g(\tilde{\omega}_z q_y - \tilde{\omega}_y q_z) \\ \Xi_{7,6} = -g(q_w^2 + q_z^2 - q_x^2 - q_y^2) \\ \Xi_{7,7} = -2g(q_w q_x + q_y q_z) \end{cases}$$

$$\begin{cases} \Xi_{8,1} = 2g(\tilde{\omega}_x q_w + \tilde{\omega}_z q_y) \\ \Xi_{8,2} = -2g(\tilde{\omega}_x q_x + \tilde{\omega}_z q_z) \\ \Xi_{8,3} = 2g(\tilde{\omega}_z q_w - \tilde{\omega}_x q_y) \\ \Xi_{8,4} = 2g(\tilde{\omega}_x q_z - \tilde{\omega}_z q_x) \\ \Xi_{8,5} = -g(q_x^2 - q_w^2 - q_z^2 + q_y^2) \\ \Xi_{8,7} = -2g(q_x q_z - q_w q_y) \end{cases} \quad \begin{cases} \Xi_{9,1} = -2g(\tilde{\omega}_x q_x + \tilde{\omega}_y q_y) \\ \Xi_{9,2} = -2g(\tilde{\omega}_x q_w - \tilde{\omega}_y q_z) \\ \Xi_{9,3} = -2g(\tilde{\omega}_y q_w + \tilde{\omega}_x q_z) \\ \Xi_{9,4} = 2g(\tilde{\omega}_y q_x - \tilde{\omega}_x q_y) \\ \Xi_{9,5} = -2g(q_w q_x + q_y q_z) \\ \Xi_{9,6} = -2g(q_w q_y - q_x q_z) \end{cases}$$

2) *Proof that the determinant of matrix  $\mathbf{A}$  is nonzero:*

After performing the derivation by cofactor expansion and assembling the resulting minors, we obtain

$$\det(\mathbf{A}) = -32g^3(q_w q_z + q_x q_y) \quad (53)$$

We express Eq. (53) using trigonometric functions. Applying the standard Z-Y-X Euler angle to quaternion conversion [46], we have

$$\begin{aligned} q_w &= c_\phi c_\theta c_\psi + s_\phi s_\theta s_\psi \\ q_x &= s_\phi c_\theta c_\psi - c_\phi s_\theta s_\psi \\ q_y &= c_\phi s_\theta c_\psi + s_\phi c_\theta s_\psi \\ q_z &= c_\phi c_\theta s_\psi - s_\phi s_\theta c_\psi \end{aligned} \quad (54)$$

where  $c_\alpha = \cos \frac{\alpha}{2}$ ,  $s_\alpha = \sin \frac{\alpha}{2}$ ,  $\alpha \in \{\psi, \theta, \phi\}$  and  $\psi, \theta, \phi$  denote heading, pitch, and roll respectively. Then, it can be readily derived that

$$\begin{aligned} q_w q_z &= (c_\phi c_\theta c_\psi + s_\phi s_\theta s_\psi)(c_\phi c_\theta s_\psi - s_\phi s_\theta c_\psi) \\ &= c_\phi^2 c_\theta^2 c_\psi s_\psi - c_\phi s_\phi c_\theta s_\theta c_\psi^2 + s_\phi c_\phi c_\theta s_\theta c_\psi^2 - s_\phi^2 s_\theta^2 s_\psi c_\psi \\ q_x q_y &= (s_\phi c_\theta c_\psi - c_\phi s_\theta s_\psi)(c_\phi s_\theta c_\psi + s_\phi c_\theta s_\psi) \\ &= s_\phi c_\phi c_\theta s_\theta c_\psi^2 + s_\phi^2 c_\theta^2 c_\psi s_\psi - c_\phi^2 s_\theta^2 s_\psi c_\psi - s_\phi c_\phi c_\theta s_\theta s_\psi^2 \end{aligned} \quad (55)$$

After some mathematic manipulations, we can obtain

$$q_w q_z + q_x q_y = \cos \theta c_\psi s_\psi = \frac{1}{2} \cos \theta \sin \psi \quad (56)$$

Substituting Eq. (56) into Eq. (53) gives the determinant of matrix  $\mathbf{A}$  as

$$\det(\mathbf{A}) = -16 g^3 \cos \theta \sin \psi \quad (57)$$

Considering the quaternion constraint  $q_w^2 + q_x^2 + q_y^2 + q_z^2 = 1$ , it follows that  $\det(\mathbf{A}) = 0$  holds only if  $\cos \theta \sin \psi = 0$ . Equivalently,  $\det(\mathbf{A})$  vanishes only if the yaw angle is  $\psi = 0^\circ$  or  $\psi = 180^\circ$ , or the pitch angle is  $\theta = \pm 90^\circ$ . In practical UAV inspection operations, the UAV's pitch angle never reaches the extreme value of  $90^\circ$ . Next, we prove that  $\psi = 0^\circ$  or  $\psi = 180^\circ$  does not influence the observability of the system. For this purpose, we choose rows  $\{1,2,3,5,7,8,9\}$  of  $\Xi$ . Notice that matrices  $\mathbf{B}$  and  $\mathbf{C}$  remain the same for this second choice of matrix  $\mathbf{A}$ , which is given by

$$\mathbf{A} = \begin{bmatrix} -2gq_y & 2gq_z & -2gq_w & 2gq_x \\ 2gq_x & 2gq_w & 2gq_z & 2gq_y \\ 2gq_w & -2gq_x & -2gq_y & 2gq_z \\ -2q_z + q_x & 2q_y + q_w & 2q_x + q_z & -2q_w + q_y \end{bmatrix} \quad (58)$$

which directly gives

$$\det(\mathbf{A}) = 16g^3(1 - 2q_w^2 - 2q_y^2) \quad (59)$$

After some mathematical derivations, we have

$$\det(\mathbf{A}) = -16 g^3(\cos \phi \cos \psi + \sin \theta \sin \phi \sin \psi) \quad (60)$$

Define  $C = \cos \phi$ ,  $D = \sin \theta \sin \phi$ , we rewrite

$$\begin{aligned} \det(\mathbf{A}) &= -16g^3(C \cos \psi + D \sin \psi) \\ &= -16g^3 \sqrt{C^2 + D^2} \cos(\psi - \delta) \end{aligned} \quad (61)$$

where  $\delta = \arctan(D, C)$ . Here,  $\arctan(\cdot, \cdot)$  denotes the two-argument arctangent function [47], which ensures correct angle

determination for all values of  $C$  and  $D$ , including the cases  $C \leq 0$ . Considering the gravity acceleration  $g > 0$ , it follows that  $\det(\mathbf{A}) = 0$  holds when  $\sqrt{C^2 + D^2} \cos(\psi - \delta) = 0$ . Note that  $\sqrt{C^2 + D^2} = \sqrt{\cos^2 \phi + \sin^2 \theta \sin^2 \phi} > 0$  for all  $(\phi, \theta)$  except the singular set  $\{\cos \phi = 0, \sin \theta = 0\}$ . In practical UAV inspection operations, the UAV's roll angle never reaches the extreme value of  $90^\circ$  thus  $\cos \phi \neq 0$ . Therefore,  $\det(\mathbf{A}) = 0$  if and only if  $\cos(\psi - \delta) = 0$ . If  $\psi = 0^\circ$  or  $\psi = 180^\circ$ ,  $\det(\mathbf{A}) = 0$  implies  $\cos(-\delta) = 0$  or  $\cos(\delta) = 0$ . However, since  $\frac{D}{C} = \sin \theta \tan \phi$  is bounded due to the physical limitations of the roll angle, i.e., it cannot reach to  $\pm 90^\circ$ , it can be concluded that  $\cos(-\delta) \neq 0$  or  $\cos(\delta) \neq 0$ . This proves that  $\det(\mathbf{A}) \neq 0$  when  $\psi = 0^\circ$  or  $\psi = 180^\circ$  for the second choice of matrix  $\mathbf{A}$ .

3) *Proof that the determinant of matrix  $\mathbf{B}$  is nonzero:* Similarly, evaluating the determinant of matrix  $\mathbf{B}$  gives

$$\begin{aligned} \det(\mathbf{B}) &= \Xi_{7,6} \Xi_{8,7} \Xi_{9,5} + \Xi_{7,7} \Xi_{8,5} \Xi_{9,6} \\ &= 8g^3(q_x^2 + q_y^2 - q_w^2 - q_z^2)(q_w q_x + q_y q_z)(q_x q_z - q_w q_y) \end{aligned} \quad (62)$$

Suppose that  $\det(\mathbf{B}) = 0$ , then it can be concluded that all three terms in the brackets of Eq. (62) should simultaneously become zero. We thus consider this condition along with the quaternion normalization constraint as

$$q_x^2 + q_y^2 - q_w^2 - q_z^2 = 0 \quad (63a)$$

$$q_w q_x + q_y q_z = 0 \quad (63b)$$

$$q_x q_z - q_w q_y = 0 \quad (63c)$$

$$q_w^2 + q_x^2 + q_y^2 + q_z^2 = 1 \quad (63d)$$

From the Eq. (63a) and Eq. (63d), we have

$$q_x^2 + q_y^2 = q_w^2 + q_z^2 \quad (64)$$

Substituting the preceding equation into the normalization constraint (63d) yields  $q_w^2 + q_z^2 = \frac{1}{2}$ . Consequently,  $q_x^2 + q_y^2 = \frac{1}{2}$ . Define two vectors in  $\mathbb{R}^2$  as  $\mathbf{a} = [q_w, q_z]$  and  $\mathbf{b} = [q_x, q_y]$ . Then, Eq. (63b) can be expressed as  $\mathbf{a} \cdot \mathbf{b}^T = 0$ . Similarly, Eq. (63c) becomes  $\mathbf{b} \cdot \mathbf{a}_\perp^T = 0$ , where  $\mathbf{a}_\perp = [q_z, -q_w]$  is orthogonal to  $\mathbf{a}$ . Since

$$|\mathbf{a}| = \sqrt{q_w^2 + q_z^2} = \sqrt{\frac{1}{2}} > 0 \quad (65)$$

vectors  $\mathbf{a}$  and  $\mathbf{a}_\perp$  form a basis for  $\mathbb{R}^2$ . However, vector  $\mathbf{b}$  is orthogonal to both basis vectors, implying  $\mathbf{b} = \mathbf{0}$ . This directly violates the condition that

$$|\mathbf{b}|^2 = q_x^2 + q_y^2 = \frac{1}{2} > 0 \quad (66)$$

Therefore, it can be concluded that  $\det(\mathbf{B}) \neq 0$  for all physically valid quaternions by contradiction.

4) *Conclusion on Observability:* According to the determinant of block triangular matrix theorem [45], the determinant of the selected submatrix is

$$\det(\mathbf{M}) = \det(\mathbf{A}) \det(\mathbf{B}) \neq 0 \quad (67)$$

As long as the UAV does not continuously remain at the specific orientations described above. Hence, the observability matrix  $\Xi$  satisfies  $\text{rank}(\Xi) = 7$ . This proves Proposition 1, establishing the local observability of the system under typical

operational conditions. Despite the theoretical possibility of rank deficiency in the observability matrix at specific singular attitudes (e.g., when the heading angle is  $0^\circ$ ,  $90^\circ$ , or  $180^\circ$ ), these points do not compromise the filter's practical performance or lead to instability. This practical robustness stems from two primary factors. On the one hand, a UAV is an inherently dynamic system subject to constant, minor corrective movements. The UAV passes these singular attitudes transiently that the filter is not exposed to any single point long enough to cause divergence. On the other hand, our observability verification method is itself robust. As demonstrated in the analysis, global observability is confirmed by verifying the rank of different submatrices. A rank drop in one specific submatrix does not imply a total loss of observability, as another submatrix can still retain full rank. This conclusion is corroborated in the subsequent experimental section, where no filter divergence or noticeable performance degradation is observed when the UAV's trajectory passed through or near these theoretical singular attitudes.

#### REFERENCES

- [1] F. Wang, B. Zhong, T. Liu, X. Kong, H. Bai, and G. Wan, "Deep matching online video stabilization using TSNet," *IEEE Trans. Instrum. Meas.*, 2024.
- [2] S. Wang, Z. Qiu, P. Huang, X. Yu, J. Yang, and L. Guo, "A bioinspired navigation system for multirotor UAV by integrating polarization compass/magnetometer/INS/GNSS," *IEEE Trans. Ind. Electron.*, vol. 70, no. 8, pp. 8526–8536, 2022.
- [3] X. Xu, Y. Sun, X. Tian, L. Zhou, and Y. Li, "A double-EKF orientation estimator decoupling magnetometer effects on pitch and roll angles," *IEEE Trans. Ind. Electron.*, vol. 69, no. 2, pp. 2055–2066, 2021.
- [4] G. He, X. Yuan, Y. Zhuang, and H. Hu, "An integrated GNSS/LiDAR-SLAM pose estimation framework for large-scale map building in partially GNSS-denied environments," *IEEE Trans. Instrum. Meas.*, vol. 70, pp. 1–9, 2020.
- [5] Z. Wang, X. Liu, L. Yang, and F. Gao, "SW-LIO: A sliding window based tightly coupled LiDAR-inertial odometry," *IEEE Robot. Autom. Lett.*, vol. 8, no. 10, pp. 6675–6682, 2023.
- [6] J. Quenzel and S. Behnke, "Real-time multi-adaptive-resolution-surfel 6D LiDAR odometry using continuous-time trajectory optimization," in *IEEE/RSJ Int. Conf. Intell. Robots Syst.* IEEE, 2021, pp. 5499–5506.
- [7] M. Wicaksono and S. Y. Shin, "GO-SLAM: GPS-aided visual inertial SLAM for adaptive UAV navigation in outdoor-indoor environments," *IEEE Trans. Instrum. Meas.*, 2025.
- [8] R. Mur-Artal and J. D. Tardós, "ORB-SLAM2: An open-source SLAM system for monocular, stereo, and RGB-D cameras," *IEEE Trans. Robot.*, vol. 33, no. 5, pp. 1255–1262, 2017.
- [9] H. Wei, T. Zhang, and L. Zhang, "A fast analytical two-stage initial-parameters estimation method for monocular-inertial navigation," *IEEE Trans. Instrum. Meas.*, vol. 71, pp. 1–12, 2022.
- [10] R. G. Valenti, I. Dryanovski, and J. Xiao, "Keeping a good attitude: A quaternion-based orientation filter for IMUs and MARGs," *Sensors*, vol. 15, no. 8, pp. 19302–19330, 2015.
- [11] M. Kok and T. B. Schön, "A fast and robust algorithm for orientation estimation using inertial sensors," *IEEE Signal Process. Lett.*, vol. 26, no. 11, pp. 1673–1677, 2019.
- [12] G. Liu, B. Yu, L. Shi, and R. Jia, "Fast and robust position and attitude estimation method based on MARG sensors," *IEEE Trans. Instrum. Meas.*, vol. 70, pp. 1–9, 2021.
- [13] G. Araguás, C. Paz, D. Gaydou, and G. P. Paina, "Quaternion-based orientation estimation fusing a camera and inertial sensors for a hovering UAV," *J. Intell. Robot. Syst.*, vol. 77, pp. 37–53, 2015.
- [14] Y. S. Suh, Y. S. Ro, and H. J. Kang, "Quaternion-based indirect kalman filter discarding pitch and roll information contained in magnetic sensors," *IEEE Trans. Instrum. Meas.*, vol. 61, no. 6, pp. 1786–1792, 2012.
- [15] L. Wohle and M. Gebhard, "SteadEye-head—improving MARG-sensor based head orientation measurements through eye tracking data," *Sensors*, vol. 20, no. 10, p. 2759, 2020.
- [16] X. Tong, M. Chen, and F. Yang, "Robust hybrid attitude and gyro-bias observer on quaternions," *IEEE Trans. Ind. Electron.*, vol. 69, no. 8, pp. 8545–8553, 2021.
- [17] M. Wei, D. Sun, S. Li, T. Zhang, and D. Wang, "Robust optimization algorithm for attitude estimation based on multi-sensor fusion under magnetic disturbance conditions," *IEEE Trans. Instrum. Meas.*, 2025.
- [18] S. O. Madgwick, A. J. Harrison, and R. Vaidyanathan, "Estimation of IMU and MARG orientation using a gradient descent algorithm," in *Proc. IEEE Int. Conf. Rehabil. Robot.* IEEE, 2011, pp. 1–7.
- [19] S. Wilson, H. Eberle, Y. Hayashi, S. O. Madgwick, A. McGregor, X. Jing, and R. Vaidyanathan, "Formulation of a new gradient descent MARG orientation algorithm: Case study on robot teleoperation," *Mech. Syst. Signal Process.*, vol. 130, pp. 183–200, 2019.
- [20] R. Costanzi, F. Fanelli, N. Monni, A. Ridolfi, and B. Allotta, "An attitude estimation algorithm for mobile robots under unknown magnetic disturbances," *IEEE/ASME Trans. Mechatronics*, vol. 21, no. 4, pp. 1900–1911, 2016.
- [21] P. Marantos, Y. Koveos, and K. J. Kyriakopoulos, "UAV state estimation using adaptive complementary filters," *IEEE Trans. Control Syst. Technol.*, vol. 24, no. 4, pp. 1214–1226, 2015.
- [22] Y. Huang, Y. Zhang, and X. Wang, "Kalman-filtering-based in-motion coarse alignment for odometer-aided SINS," *IEEE Trans. Instrum. Meas.*, vol. 66, no. 12, pp. 3364–3377, 2017.
- [23] S. Xu and K. Doğançay, "Optimal sensor placement for 3-D angle-of-arrival target localization," *IEEE Trans. Aerosp. Electron. Syst.*, vol. 53, no. 3, pp. 1196–1211, 2017.
- [24] B. Kada, K. Munawar, M. Shaikh, M. Hussaini, and U. Al-Saggaf, "UAV attitude estimation using nonlinear filtering and low-cost MEMS sensors," *IFAC-PapersOnLine*, vol. 49, no. 21, pp. 521–528, 2016.
- [25] Y. Xu, J. Quo, and Y. Guan, "EKF based multiple-mode attitude estimator for quadrotor using inertial measurement unit," in *Proc. 36th Chinese Control Conf.* IEEE, 2017, pp. 6191–6198.
- [26] W. Lin, S. Ding, Z. Li, and N. Yang, "A three-step calibration method of sensors' pose for magnetic localization system," *IEEE Trans. Instrum. Meas.*, vol. 72, pp. 1–10, 2023.
- [27] J. Lee, J. Lim, and J. Lee, "Compensated heading angles for outdoor mobile robots in magnetically disturbed environment," *IEEE Trans. Ind. Electron.*, vol. 65, no. 2, pp. 1408–1419, 2017.
- [28] M. L. Hoang and A. Pietrosanto, "Yaw/Heading optimization by machine learning model based on MEMS magnetometer under harsh conditions," *Measurement*, vol. 193, p. 111013, 2022.
- [29] H. Li, S. Chang, Q. Yao, C. Wan, G.-J. Zou, and D.-L. Zhang, "Robust heading and attitude estimation of MEMS IMU in magnetic anomaly field using a partially adaptive decoupled extended Kalman filter and LSTM algorithm," *IEEE Trans. Instrum. Meas.*, vol. 73, pp. 1–13, 2024.
- [30] F. Bo, J. Li, W. Wang, and K. Zhou, "Robust attitude and heading estimation under dynamic motion and magnetic disturbance," *Micromachines*, vol. 14, no. 5, p. 1070, 2023.
- [31] F. Huang, Z. Wang, L. Xing, and C. Gao, "A MEMS IMU gyroscope calibration method based on deep learning," *IEEE Trans. Instrum. Meas.*, vol. 71, pp. 1–9, 2022.
- [32] M. Brossard, S. Bonnabel, and A. Barrau, "Denoising IMU gyroscopes with deep learning for open-loop attitude estimation," *IEEE Robot. Autom. Lett.*, vol. 5, no. 3, pp. 4796–4803, 2020.
- [33] S. Herath, H. Yan, and Y. Furukawa, "Ronin: Robust neural inertial navigation in the wild: Benchmark, evaluations, & new methods," in *IEEE Int. Conf. Robot. Autom.* IEEE, 2020, pp.

- 3146–3152.
- [34] M. A. Esfahani, H. Wang, K. Wu, and S. Yuan, “OriNet: Robust 3-D orientation estimation with a single particular IMU,” *IEEE Robot. Autom. Lett.*, vol. 5, no. 2, pp. 399–406, 2019.
  - [35] W. Liu, D. Caruso, E. Ilg, J. Dong, A. I. Mourikis, K. Daniilidis, V. Kumar, and J. Engel, “Tlio: Tight learned inertial odometry,” *IEEE Robot. Autom. Lett.*, vol. 5, no. 4, pp. 5653–5660, 2020.
  - [36] A. M. Sabatini, “Quaternion-based extended Kalman filter for determining orientation by inertial and magnetic sensing,” *IEEE Trans. Biomed. Eng.*, vol. 53, no. 7, pp. 1346–1356, 2006.
  - [37] R. Kanwal and K. Liu, “A Taylor expansion approach for solving integral equations,” *Int. J. Math. Educ. Sci. Technol.*, vol. 20, no. 3, pp. 411–414, 1989.
  - [38] J. H. Cartwright and O. Piro, “The dynamics of Runge-Kutta methods,” *Int. J. Bifurcation Chaos*, vol. 2, no. 03, pp. 427–449, 1992.
  - [39] S. Xu, K. Doğançay, and H. Hmam, “Distributed pseudolinear estimation and UAV path optimization for 3D AOA target tracking,” *Signal Process.*, vol. 133, pp. 64–78, 2017.
  - [40] C. Song, Z. Huang, Y. Wu, S. Li, and Q. Chen, “An innovation-based adaptive cubature Kalman filtering for GPS/SINS integrated navigation,” *IEEE Sensors J.*, 2024.
  - [41] R. Hermann and A. Krener, “Nonlinear controllability and observability,” *IEEE Trans. Autom. Control*, vol. 22, no. 5, pp. 728–740, 1977.
  - [42] D. Laidig and T. Seel, “VQF: Highly accurate IMU orientation estimation with bias estimation and magnetic disturbance rejection,” *Inf. Fusion*, vol. 91, pp. 187–204, 2023.
  - [43] Q. Zhang, H. Pang, and C. Wan, “Magnetic interference compensation method for geomagnetic field vector measurement,” *Measurement*, vol. 91, pp. 628–633, 2016.
  - [44] T. Seel and S. Ruppin, “Eliminating the effect of magnetic disturbances on the inclination estimates of inertial sensors,” *IFAC-PapersOnLine*, vol. 50, no. 1, pp. 8798–8803, 2017.
  - [45] R. A. Horn and C. R. Johnson, *Matrix Analysis*, 2nd ed. Cambridge Univ. Press, 2012.
  - [46] J. B. Kuipers, *Quaternions and rotation sequences: a primer with applications to orbits, aerospace, and virtual reality*. Princeton Univ. Press, 1999.
  - [47] R. Zhang, H. Liu, Y. Zhou, Z. Yang, and J. Han, “Design and analysis of a mutual inductance coupling-based microdeformation sensor,” *IEEE Trans. Instrum. Meas.*, vol. 66, no. 4, pp. 821–829, 2017.